Energy Reports 8 (2022) 7704–7711

Contents lists available at ScienceDirect

Energy Reports

journal homepage: www.elsevier.com/locate/egyr

Research paper

Enhancement of power system stability by real-time prediction of instability and early activation of steam turbine fast valving

Sylwester Robak *, Jan Machowski, Mateusz Skwarski

Warsaw University of Technology, Faculty of Electrical Engineering, Poland

A R T I C L E I N F O

Article history:
Received 21 March 2022
Received in revised form 9 May 2022
Accepted 31 May 2022
Available online 17 June 2022

Keywords:
Fast valving
Stability analysis
Severe contingency events
Real-time instability prediction
Smart control schemes

A B S T R A C T

Turbine FV is a stability enhancing method used to protect power systems against the loss of synchronism after extreme contingency events. To avoid unnecessary FV action, smart control schemes can be used based on real-time instability prediction. In the last decade, several WAMS-based instability prediction methods have been developed. However, relatively long cumulative latencies in WAMS structures significantly reduce the efficiency of preventive control and can lead to system instability. To speed up FV action initiated by smart control scheme, this paper proposes a fast stability prediction method which is completely different from other methods described in literature. It uses only local measurements and requires performing simple mathematical operations. The basis of this method is the prediction of the magnitude of the power-angle characteristic. Just after the fault clearance, the method allows to predict transient instability and initiate MFV action. Based on the magnitude of the power-angle characteristic, the steady-state stability margin can be also computed. When this margin is too small, SFV action can be initiated as well. The validity of the proposed method has been verified by simulations performed for a large-scale real power system and detailed models of power system elements.

1. Introduction

Power systems should be capable of meeting consumer demand while surviving contingencies without violation of performance standards related to thermal, voltage, frequency and stability limits. A contingency is defined as an event which cannot be predicted in advance, e.g., a short circuit in the network and its clearance followed by a loss of a single or several network elements. Dynamic performance of each power system depends on the severity of the contingency event (Kundur, 1994; Machowski et al., 2020).

To limit the risk of cascade tripping in the transmission network and/or power system instability after severe contingencies, transmission system operators implement various event-based controls and protections referred to as special protection schemes (NERC, 2013). A review of stability improvement methods can be found in book (Machowski et al., 2020), brochure (CIGRE, 2007), and papers (Pertl et al., 2017; CIGRE, 2018).

Overloads inside a meshed network can be alleviated by generation rescheduling or by network or busbars splitting. Overloads in the transmission network connecting the power plant to other parts of the system can be alleviated by generation curtailment by partial-load rejection or, in heavy overloads, by generator tripping (Cong et al., 2016; Robak et al., 2018).

Special protection schemes developed to prevent the loss of synchronism in power systems after severe contingencies include generator tripping and fast valving.

Tripping some generating units operating on the same busbar is very effective in braking the generator rotors losing synchronism after a severe fault in the network (Machowski et al., 2020; Karady and Gu, 2002). However, generator tripping has some drawbacks (Kundur, 1994). It causes power imbalance which must be corrected by automatic generation control or load shedding. For multiunit power plants, when some generating units are tripped, the remaining units experience high levels of shaft torque and shaft fatigue. Therefore, the use of generator tripping is limited to multiunit power plants with small or medium-sized generating units operating on the same busbar. For power plants with few but large generating units, the use of generator tripping is not reasonable, and fast valving is used instead.

Fast valving (FV) assists in maintaining power system transient stability following a severe fault by reducing the turbine power (Kundur, 1994; Machowski et al., 2020). It can be performed as momentary fast valving (MFV) or sustained fast valving (SFV). For MFV, only the intercept valves are closed for an adjustable period and then are reopened to restore turbine power

* Correspondence to: ul. Koszykowa 75, 00-662 Warsaw, Poland.
E-mail address: Sylwester.Robak@pw.edu.pl (S. Robak).

https://doi.org/10.1016/j.egyr.2022.05.285

Abbreviations

AVR	Automatic voltage regulator
CCT	Critical clearing time
EMF	Electromotive force
FV	Turbine fast valving
MFV	Momentary fast valving
PSS	Power system stabilizer
SFV	Sustained fast valving
SMIB	Single machine-infinite busbar
SPS	Special protection scheme
WAMS	Wide area measurement system

to its pre-fault value. For SFV, the main control valves are also partially closed in order to reduce turbine power in the post-fault state to a required value smaller than in the pre-fault state. If the required reduction of turbine power by SFV is more than 10%–20%, bypass valving must be also activated and correctly coordinated with turbine control (Patel et al., 2001).

The speed with which turbine valve reopens during MFV is limited by the strength of turbine rotor blades (Kundur, 1994; Machowski et al., 2020). Typically, restoration of turbine power takes several seconds, which is too slow when compared to fast changes in electrical real power of the generator. As a result, MFV causes a deep rotor backward swing that can reach the motoring range of the generator operation (negative electrical real power). To prevent such situation and improve damping of power swings, it is recommended to support MFV by rapid control of the excitation voltage control by the AVR equipped with PSS. The influence of PSS on transient state following MFV is described in book (Machowski et al., 2020).

Review paper (Patel et al., 2001) describes experiences, benefits and problems associated with fast valving applied to various types of fossil-fired and nuclear power plants. Possible adverse effects of FV on the turbine and steam generator are described in book (Kundur, 1994). In view of these adverse effects, the FV action should be initiated only where after a given fault the loss of synchronism is very likely. For this reason, the method to initiate FV action is of crucial importance.

In standard control circuitry offered by turbine manufacturers, FV action is usually initiated by a power load unbalance logic, which is an extension of the logic used to limit overspeed (Kundur, 1994; Prioste et al., 2004; Cai et al., 2017). Unfortunately, such simple logic may lead to an unnecessary FV action. To avoid this, additional SPS should be used that can identify the faults that actually require FV action.

The initial types of such SPSs, also in use today, have been based on look-up tables and off-line preprogrammed logic based on multi-variant off-line stability analysis (Machowski et al., 2020). An important disadvantage of this type of SPSs is a limited possibility of real-time adaptation. However, alternative and more advanced smart control schemes are available which utilize fast instability prediction.

Papers (Wu et al., 2011; Li et al., 2019; Sobbouhi and Vahedi, 2021) contain a broad review of various instability prediction methods. Recently published papers (Zhou et al., 2019; Lv and Pawlak, 2019) describe instability prediction methods based on neural network and multivariate regression function.

Due to rapid development of wide area measurement systems (WAMS), most of instability prediction methods described in literature of the last decade are based on phasor measurement units (PMU). Paper (Wang and He, 2019) reports that WAMS-based dynamic security assessment and smart control schemes implemented in real-world power systems have been based on a single machine so far-infinite busbar (SMIB) equivalent model. Most of such schemes are basically various modifications of the instability prediction method originally described in book (Pavella et al., 2000). The instability prediction method described in this paper is also based on the SMIB equivalent model, but is different from other known methods. The proposed method does not use system trajectory or parameters of simplified equivalent model of power system for instability prediction, but uses the magnitude of power-angle characteristic instead. The proposed method has been verified by computer simulation using a precise model of a large-scale real-world power system.

2. Motivation

Although there has been a prevailing enthusiasm about smart control schemes based on WAMS, some recently published papers report that cumulative latencies in WAMS structures significantly decrease the control efficiency and, in the case of closed loop control using phasors from PMUs, can lead to system instability (Molina-Cabrera et al., 2021).

All causes and components of latency in WAMS structures are defined and discussed in detail in report (CIGRE, 2017). Very recently published paper (Molina-Cabrera et al., 2021) presents an interesting statistical analysis and shows that a significant number of PMU data arrive to the control scheme after 200–350 ms and there are outliers with even higher delays. Paper (Zweigle and Venkatasubramanian, 2016) describes a very sophisticated WAMS-based control system used to improve transient stability by generator tripping and estimates that the cumulative latency in the considered system is about 200 ms.

For SPSs that must decide about initiation of FV operation such delays are too long. This fact is a strong motivation to develop a fast instability prediction method and a smart control scheme based on local measurements only. This paper presents such an approach.

3. Prediction of instability

After extreme faults, power systems lose their transient stability during the first swing of the generators closest to the short circuit. The first-swing instability can be recognized using simple power system model in which a group of synchronous generators operating in the power system is represented by the SMIB model.

3.1. SMIB equivalent model

The circuit diagram of the SMIB model is shown in Fig. 1. In this diagram, X'_d, $\underline{E}$, $\underline{V}_G$, P, Q are the transient reactance, electromotive force, terminal voltage, active and reactive powers of the equivalent generator, respectively. X_T is reactance of the step-up transformer. The remaining part of the system is represented by the source of voltage $\underline{V} = \text{const}$ and equivalent reactance X_S. The difference between the phase angles of $\underline{E}$ and $\underline{V}$ is referred to as power angle δ. $X_G = X'_d + X_T$ is the equivalent reactance of the generating unit (generator plus step-up transformer).

The rotor motion of the equivalent generator in the SMIB model is described by the following differential equation:

$$M\frac{\mathrm{d}\Delta\omega}{\mathrm{d}t} = P_m - P \tag{1}$$

where $M = T_m S_n/\omega_s = 2HS_n/\omega_s$ is the coefficient of inertia, $\Delta\omega = \mathrm{d}\delta/\mathrm{d}t$ is the deviation of speed, P_m is the mechanical power, and P is the electrical power expressed by the following formula (Machowski et al., 2020):

$$P = \frac{EV}{X}\sin\delta = P_{max}\sin\delta \tag{2}$$

where $X = X_G + X_S$ and $P_{max} = EV/X$ is the magnitude of the power-angle characteristic $P(\delta)$ shown in Fig. 1.

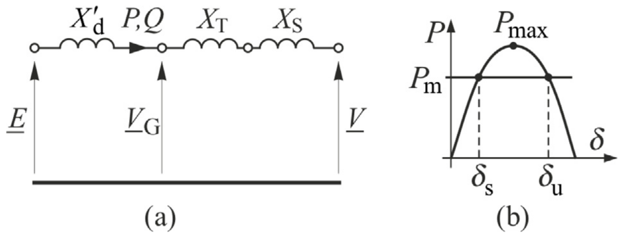

Fig. 1. Illustration of the SMIB model: (a) circuit diagram and (b) power-angle characteristic $P(\delta)$.

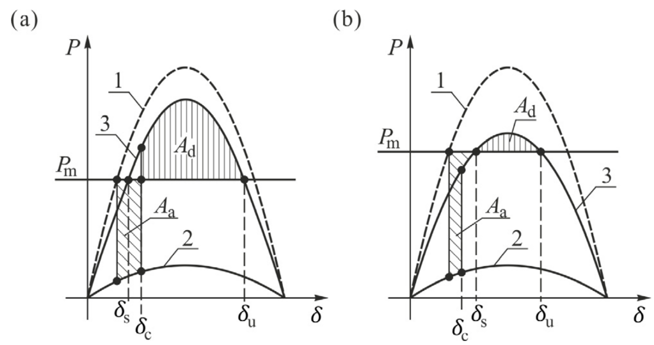

Fig. 2. Acceleration and deceleration areas for two different post-fault states: (a) for $P_c \geq P_m$, (b) for $P_c < P_m$.

3.2. Energy-based stability condition

The system described by Eqs. (1) and (2) is nonlinear, and its transient stability depends on the type of the fault, its duration and electrical distance from the generator (Machowski et al., 2020).

The first-swing instability can be predicted by using energy-based method derived from the direct Lyapunov method and referred to as the equal-area method (Machowski et al., 2020; Pavella et al., 2000). For the purpose of this paper, the equal-area method is illustrated in Fig. 2, which shows the power-angle characteristics for three states: 1 — the pre-fault state, 2 — the fault state, and 3 — the post-fault state. δ_c is the power angle at the moment t_c of the fault clearance and δ_s, δ_u are coordinates of the post-fault stable and unstable equilibrium points.

Area A_a hatched with the sloping lines is proportional to the surplus of the kinetic energy released by the fault and is referred to as the acceleration area. Area A_d hatched with the vertical lines is referred to as the available deceleration area and represents the ability of the power system to maintain transient stability. For the given pre-fault state and given fault the power system is stable (i.e. synchronism is preserved) if the following condition is met:

$$A_d > A_a \tag{3}$$

In such case, the transient stability margin

$$k_{A\%} = \frac{A_d - A_a}{A_d} \cdot 100\% \tag{4}$$

is positive. If $A_d < A_a$, the system is unstable.

The steady-state stability margin is defined in the following way:

$$k_{P\%} = \frac{P_{max} - P_m}{P_m} \cdot 100 \tag{5}$$

When this margin is smaller than the value required by the power system performance standard, turbine power must be reduced to $P_{m\infty}$ for which $k_{P\%}$ is more than or equal to the required value.

3.3. Real-time calculation of areas A_a and A_d

Assuming that for the post-fault state the magnitude P_m of the power angle characteristic is known, the coordinates of the equilibrium points and power angle at the moment of the fault clearance can be calculated from the following equations:

$$\delta_s = \arcsin(P_m/P_{max}) \quad \text{and} \quad \delta_u = (\pi - \delta_s) \tag{6}$$

$$\delta_c = \arcsin(P_c/P_{max}) \tag{7}$$

The formulas used for calculating areas A_a and A_d vary in individual cases shown in Fig. 2 as described below.

Case (a) — Fig. 2a

In this case, the acceleration area A_a is proportional to the surplus of the kinetic energy released by the fault:

$$A_a = \frac{1}{2} M \cdot \Delta\omega_c^2 \tag{8}$$

where $\Delta\omega_c$ is the speed deviation at the moment of fault clearance.

The available deceleration area A_d can be determined as the integral of the difference in the power-angle characteristic $P(\delta)$ and mechanical power P_m from angle δ_c to unstable equilibrium point δ_u:

$$A_d = \int_{\delta_c}^{\delta_u} P_{max} \sin\delta \, d\delta - P_m \cdot (\delta_u - \delta_c) \tag{9}$$

and hence:

$$A_d = P_{max}(-\cos\delta_u + \cos\delta_c) - P_m(\delta_u - \delta_c) \tag{10}$$

where δ_c and P_c are the power angle and active power at moment t_c.

Case (b) — Fig. 2b

In this case, after the fault is cleared, the rotor is still accelerated and the acceleration area must be increased by:

$$\Delta_a = P_m(\delta_s - \delta_c) - \int_{\delta_c}^{\delta_s} P_{max} \sin\delta \, d\delta \tag{11}$$

The resultant acceleration area is equal to the sum of the right-hand sides of Eqs. (8) and (11):

$$A_a = \frac{1}{2} M \cdot \Delta\omega_c^2 + P_m(\delta_s - \delta_c) - P_{max}(\cos\delta_c - \cos\delta_s) \tag{12}$$

where δ_s and δ_c are given by Eqs. (6) and (7).

In this case, the available deceleration area lies between points δ_s and $\delta_u = (\pi - \delta_s)$:

$$A_d = \int_{\delta_s}^{\delta_u} P_{max} \sin\delta \, d\delta - P_m(\delta_u - \delta_s) \tag{13}$$

Hence, considering that $\cos\delta_u = -\cos\delta_s$, the following is obtained:

$$A_d = 2P_{max}\cos\delta_s - P_m(\pi - 2\delta_s) \tag{14}$$

4. Real-time identification of P_{max}

The above equations indicate that the magnitude of the power-angle characteristic P_{max} is the key parameter. Its identification soon after the fault clearance enables predicting the instability of the power system. Obviously, for the purpose of real-time instability prediction, P_{max} cannot be calculated directly from Eq. (2) because the equivalent reactance X and voltage of the infinite bus V are not known.

A new method is derived below, which makes it possible to identify P_{max} in real time based on local measurements such as rotor speed deviation $\Delta\omega$, generator terminal voltage $\underline{V}_G$ and active and reactive generator power P, Q.

4.1. Mathematical background

From Eq. (2), it follows that:

$$(P_{\max}\sin\delta)^2 = P^2 \tag{15}$$

The rate of change of the active power during power swings after the fault clearance is equal to the time derivative:

$$\frac{\mathrm{d}P}{\mathrm{d}t} = \frac{\partial P}{\partial \delta}\cdot\Delta\omega + \frac{\partial P}{\partial E}\cdot\frac{\mathrm{d}E}{\mathrm{d}t} \tag{16}$$

where:

$$\frac{\partial P}{\partial \delta} = P_{\max}\cos\delta; \qquad \frac{\partial P}{\partial E} = \frac{V}{X}\sin\delta = \frac{P}{E} \tag{17}$$

Insertion of Eqs. (17) into Eq. (16) gives the following:

$$\frac{\mathrm{d}P}{\mathrm{d}t} = P_{\max}\cos\delta\cdot\Delta\omega + \frac{P}{E}\cdot\frac{\mathrm{d}E}{\mathrm{d}t} \tag{18}$$

and hence:

$$(P_{\max}\cos\delta)^2 = \left[\frac{\mathrm{d}P}{\mathrm{d}t} - \frac{P}{E}\cdot\frac{\mathrm{d}E}{\mathrm{d}t}\right]^2\cdot\frac{1}{(\Delta\omega)^2} \tag{19}$$

The sum of the squares of sine and cosine is 1, and therefore, it follows from the sum of Eqs. (15) and (19) that:

$$P_{\max}^2 = P^2 + \left(\frac{\mathrm{d}P}{\mathrm{d}t} - \frac{P}{E}\cdot\frac{\mathrm{d}E}{\mathrm{d}t}\right)^2\cdot\frac{1}{(\Delta\omega)^2} \tag{20}$$

At each moment of the transient state, electromotive force E may be calculated based on voltage drop across the transient generator reactance (Fig. 1):

$$\underline{E} = \underline{V}_{\mathrm{G}} + \frac{X'_{\mathrm{d}}Q}{V_{\mathrm{G}}} + \mathrm{j}\frac{X'_{\mathrm{d}}P}{V_{\mathrm{G}}} \quad \text{and} \quad E = \left|\underline{E}\right| \tag{21}$$

where j is the angular shift by $\pi/2$ and V_{G}, P, Q are the terminal voltage and the active and reactive generator powers, respectively.

Assuming that transient electromotive force does not change by much and the rate of change is small, Eq. (20) can be simplified in the following way:

$$P_{\max}^2 \cong P^2 + \left(\frac{\mathrm{d}P}{\mathrm{d}t}\right)^2\cdot\frac{1}{(\Delta\omega)^2} \tag{22}$$

However, Eq. (22) gives good approximation only for slow exciters with big time constants (e.g. cascaded DC generators). For fast exciters with small time constant (e.g. thyristor controlled rectifiers) Eq. (22) may provide too big value of $P_{\max}$. Therefore, in general case Eq. (20) is recommended.

Mathematical operations in Eqs. (20) and (22) are not feasible if $\Delta\omega = 0$. However, this is not a problem for predicting, because, soon after the fault clearance, speed deviation is always positive, $\Delta\omega > 0$.

4.2. Measurement aspects

From the point of view of instability prediction, the above-described identification of $P_{\max}$ should start as soon as possible after the fault clearance. However, in AC networks, all switching operations are accompanied by sudden changes in electrical quantities and fast transients of measured instantaneous values. Hence, the measurement of electrical quantities P, Q, V_{G} must be performed with digital fast algorithms washing out fast transients e.g. algorithms based on orthogonal decomposition of measured signals. Such algorithms and their dynamic properties are described in book (Rebizant et al., 2011). For this paper and instability prediction based on local measurements, it is important to consider that, after fault clearance, full-cycle finite impulse response (FIR) digital algorithms provide accurate values after one cycle of the fundamental frequency (20 ms for the 50 Hz AC systems).

Time derivatives $\mathrm{d}P/\mathrm{d}t$ and $\mathrm{d}E/\mathrm{d}t$ can be computed using the forward Euler method:

$$\left.\frac{\mathrm{d}P}{\mathrm{d}t}\right|_i = \frac{P_{i+1}-P_i}{t_{i+1}-t_i} \quad \text{and} \quad \left.\frac{\mathrm{d}E}{\mathrm{d}t}\right|_i = \frac{E_{i+1}-E_i}{t_{i+1}-t_i} \tag{23}$$

where i denotes the number of the consecutive sampling period. For example, when sampling frequency in the measuring instruments is 1000 Hz, the sampling period is 1 ms. Values computed from Eqs. (23) may be smoothed out by a half-cycle low pass filter. For AC systems with fundamental frequency 50 Hz, this involves a delay of about 10 ms.

Cumulative delay resulting from the washing out of fast transients and the smoothing out of the measured values is about 1.5 cycle (i.e. 30 ms for AC systems with fundamental frequency 50 Hz).

5. Smart special protection scheme

The above-described methods of instability prediction and identification of $P_{\max}$ can be applied to a smart SPS initiating MFV and SFV. The operation of the proposed SPS is described by the flowchart shown in Fig. 3.

Block 1 of this flowchart concerns measurements of the quantities needed for instability prediction and identification of $P_{\max}$.

Block 2 collects signals form digital distance protections of transmission lines connecting the power plant to the remaining part of the system.

Contemporary distance protections have several zones and one of them (referred to as the short zone) may be used to detect 3-phase faults close to the busbars of the substation. Such faults are the most dangerous for transient stability and it is reasonable to assume that MFV is initiated immediately when a 3-phase fault is recognized in the short zone. The logical variable m used in the flowchart distinguishes between states in which MFV has already been initiated $m = 1$ and has not been initiated $m = 0$.

Block 3 is optional and may be activated by the user or not. In paper (Robak et al., 2020), similar short zones are used to modify the logic of the breaker failure protection. When the optional block 3 is not activated or in the case of other faults cleared with normal or delayed clearing time, MFV is initiated in block 7 after the instability prediction performed in block 6.

Detection of fault clearance in block 4 may be realized using the output signals from protection devices and auxiliary contacts of the circuit breaker. Additionally, the initiation procedure may be augmented by recognizing a sudden change in reactive power as described in Kobayashi et al. (2011).

For all faults in transmission lines connecting the given power plant to the remaining part of the system, the value of $P_{\max}$ is identified and, in block 5, margins $k_{\mathrm{A\%}}$ and $k_{\mathrm{P\%}}$ are computed from Eqs. (4) and (5), respectively. Momentary fast valving (MFV) is activated when $k_{\mathrm{A\%}} < \varepsilon_{\mathrm{A\%}}$, where $\varepsilon_{\mathrm{A\%}}$ is a small positive number depending on cumulative error of current and voltage transformers and measuring devices.

When margin $k_{\mathrm{P\%}}$ is too small, then, in block 8, a reduced value of the turbine power $P_{\mathrm{m}\infty} = rP_{\mathrm{m}}$ is calculated:

$$P_{\mathrm{m}\infty} = rP_{\mathrm{m}} = \frac{P_{\max}}{k_{\mathrm{P\%(min)}}/100 + 1} \tag{24}$$

where r is the reduction coefficient, $k_{\mathrm{P\%(min)}}$ is a value required by the performance standards. Reduction of turbine power is performed in block 9 by partial closing of the control valve, what is referred to as sustained fast valving (Machowski et al., 2020).

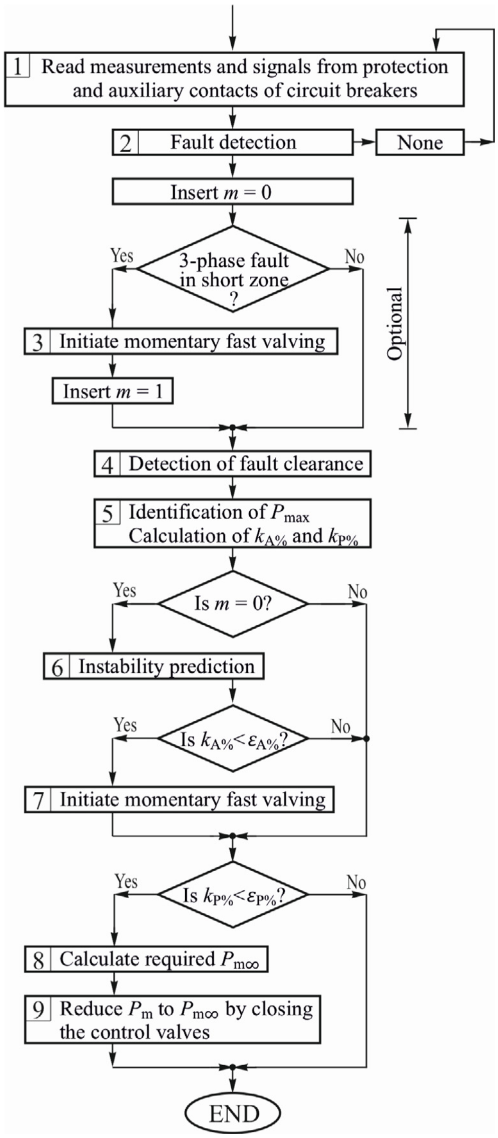

Fig. 3. Flowchart of the proposed SPS.

6. Simulation tests

6.1. Test system

Simulation tests were performed for a real-life power system with a capacity of 28,900 MW, which is a subsystem of a large-scale interconnected power system with a capacity of 166,700 MW. A model of such interconnected system includes 5883 buses, 6860 lines, 939 transformers, 50 shunt compensators, and 629 synchronous generators. The data of this system can be downloaded from report (ENTSO-E, 2015).

6.2. Power plant and substation considered

In the fossil-fuel power plant considered here, two large generating units G1 and G2 with power rating 1500 MVA (1350 MW) currently operate at a 400 kV substation. The layout of this substation is shown in Fig. 4. Three transmission lines L1, L2, L3 connect this substation to the remaining part of the system. In the future, the power plant and its substation will be expanded (dotted lines in Fig. 4) to include generating unit G3 and transmission line L4. Moreover, the local sub-transmission network 220 kV will be connected to this substation via transformer T1 (500 MVA). Simulation tests described below have been performed for the current configuration (solid lines in Fig. 4).

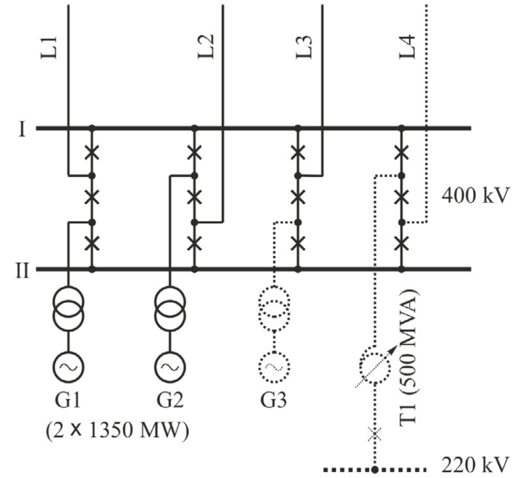

Fig. 4. Substation layout of the considered power plant × circuit breaker in the closed position.

In the simulation tests, the synchronous generators G1 and G2 are represented by GENROU model (Weber, 2015). Exciters of these generators are of the static type (thyristor-controlled rectifier) supplied from the generator terminals. Voltage controllers of the generators are equipped with dual-input stabilizers with speed deviation and active power as the input signals. In simulations, the AVR and PSS were represented by models ST1 A and PSS2B (Anon, 2016). Steam turbines of both generating units were represented in simulation by model TGOV3 with the MFV procedure (Anon, 2013). The SFV of the control valves was modeled in TGOV3 by ramping up P_{ref} from P_m to $P_{m\infty}$.

The substation considered here (Fig. 4) has the One and A Half Breaker Bus configuration and is equipped with two-cycle circuit breakers. All lines are protected by one-cycle protections. However, based on the available statistical data, the normal clearing time is further assumed to be $t_c = 80$ ms, where 30 ms is assumed for protections and 50 ms for circuit breakers.

6.3. Assessment of the steady-state stability margin

For the pre-fault state, the performance standard described in book (Machowski et al., 2020) recommends a steady-state stability margin of $k_{P\%} \geq 20\%$. For the power plant considered here, such condition is met, which can be proved using simulation results shown in Fig. 5. The critical clearing time for a 3-phase temporary fault at the busbars is $t_{CCT} = 131$ ms. The waveforms shown in this figure are for the temporary 3-phase faults cleared at 130 ms $< t_{CCT}$ and 132 ms $> t_{CCT}$, respectively.

For deep synchronous swings (Fig. 5a), the rotor angle $\delta(t)$ passes through the top of the power angle characteristic P_{max} two times, once during forward motion and once during backward motion. As a result, the power waveform $P(t)$ exhibits characteristic humps, which disappear as the oscillations are damped out (Machowski et al., 2020). In Fig. 5a, the second top P_{max} of the power angle characteristic is higher than the first one because of increased excitation voltage and transient EMF.

For asynchronous swings (Fig. 5b), the rotor angle $\delta(t)$ passes through the top P_{max} of the power angle characteristic during each asynchronous rotation. The first top P_{max} is approximately the same as for deep synchronous swings (Fig. 5b). Therefore,

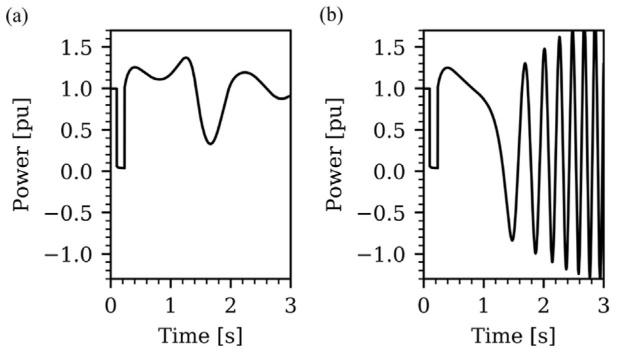

Fig. 5. The waveforms of active power $P(t)$ for: (a) deep synchronous swings (b) asynchronous swings.

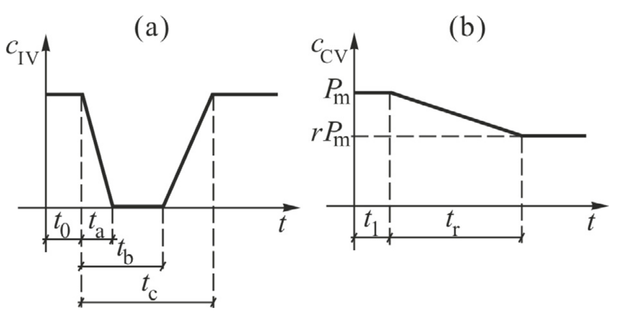

Fig. 6. Variations in the valve position: (a) position of the intercept control valves c_{IV}, (b) position of the main control valves c_{CV}.

from the point of view of the calculation of the steady-state stability margin or prediction of the transient instability, the first top P_{max} of power-angle characteristic is important.

Based on Fig. 5 and numerical values $P(t)$ obtained by simulation, it can be assumed that in the pre-fault state $P_{max} \cong 1.25$ pu. For such value, the steady-state stability margin is $k_{P\%} \cong 25\%$.

6.4. Fast valving parameters

Fig. 6 illustrates definitions of FV parameters used in the simulation test described below.

Parameters of the MFV model used in TGOV3 model are defined in Fig. 6a. The following values were used: $t_a = 0.15$ s, $t_b = 0.35$ s, $t_c = 9$ s. Some references (e.g. Kundur, 1994) recommend much faster opening of the intercept valves, but authors of this paper are of opinion that fast opening is dangerous for turbine blades. Moreover, a slower recovery of turbine power allows the AVR+PSS to damp out power swings during a few seconds.

SFV has been modeled by ramping (Fig. 6b) of the reference value P_{ref} of turbine power. Time t_r to reduce P_{ref} depends on the required reduction and is about several seconds in the case of a small reduction.

6.5. Example with the short-zones option activated

Fig. 7 shows that critical clearing time t_{CCT} increases significantly with the fault distance. Based on this figure, it may be assumed that in the option with short zones (Fig. 3) the reach of the short zone could be set to 15% of the line length for both line L2 and 8% for line L3. For line L1, the SPS (Fig. 3) may operate without the short zones option, because $t_{CCT} > 80$ ms for this line.

Simulation results for a 3-phase fault in line L2 close to the busbars 400 kV are shown in Fig. 8. In this case the fault is assumed to appear at $t = 0.1$ s and be cleared after $t_c = 0.08$ s

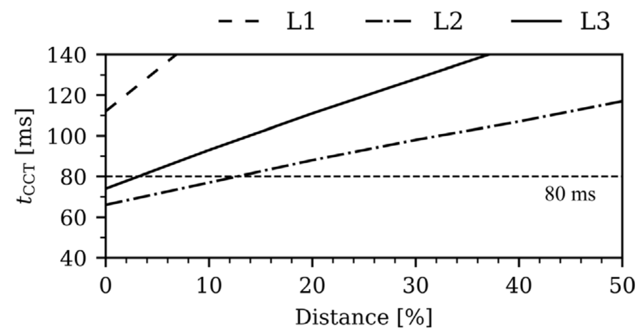

Fig. 7. Relationship between t_{CCT} and the fault distance.

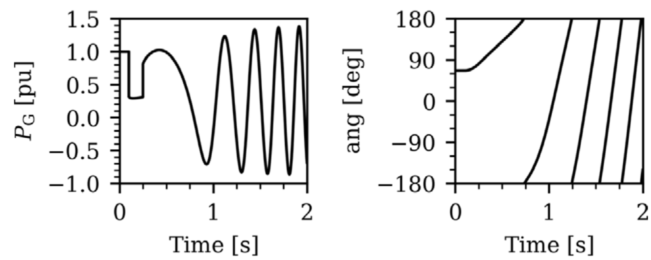

Fig. 8. The waveforms for 3-phase fault in line L2 close to the busbars without the use of MFV.

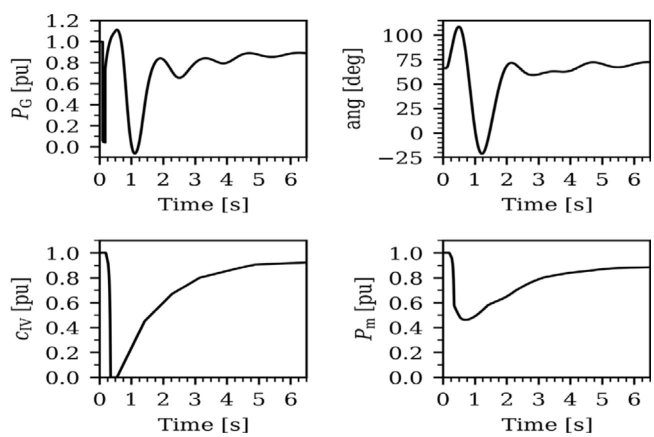

Fig. 9. Waveforms for a 3-phase fault in line L2 close to the busbars and MFV activated by the short-zones option.

i.e. at $t = 0.18$ s. If MFV is not activated, the generators lose synchronism and the system becomes unstable. The waveform $P(t)$ shown in Fig. 8 is characterized by fast changes from plus to minus, which is typical for asynchronous operation (Machowski et al., 2020). During asynchronous rotations, $\delta(t)$ permanently increases, which is shown in Fig. 8 as alternating changes from -180 deg to $+180$ deg.

Fig. 9 shows simulation results for the same fault, but in the case when MFV is initiated by the SPS with the short-zones option activated. In such a case, the tripping command is fed to the circuit breaker and additionally to the SPS (Fig. 3) in order to initiate MFV. The intercept valves are fully closed at $(t_0 + t_a) = 0.28$ s. The intercept valves begin to open at $(t_0 + t_b) = 0.48$ s. In the meantime, the fault is cleared by switching off the faulted line L2 at $(t_0 + 0.050)$ s $= 0.18$ s. During 30 ms after the fault clearance, the SPS (using the above-described prediction method) predicts for the post-fault state the magnitude of the power-angle characteristic $P_{max} \cong 1.098$ pu. This means that, without a reduction of the mechanical power $P_m = 1$ pu, the steady-state

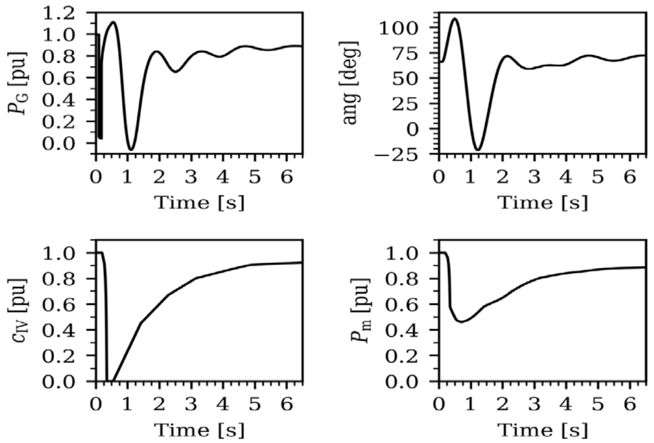

Fig. 10. Waveforms for 3-phase fault in line L2 close to the busbars and MFV initiated by instability prediction without using the short-zones option.

stability margin in the post-fault state would be $k_{P\%} = 9.8\%$. As it results from Eq. (24), to restore the 20% stability margin, the SPS must reduce mechanical power to $P_{m\infty} = 0.915$ pu. Such reduction is performed (Fig. 3) by SFV by partial closing of the main control valves.

6.6. Example with the short-zones option not activated

When the short-zones option is not activated, MFV is initiated by the SPS (Fig. 3) after fault clearance, based on instability prediction. The example described below illustrates such a case.

In case of the 3-phase fault in L2 close to the busbars the following values have been obtained after the fault clearance:

$P_m = 1$ pu, $P_c = 0.759$ pu, $\Delta\omega = 2.35$ rad/s

$P_{max} = 1.098$ pu, $A_a = 0.117$ pu · rad, $A_d = 0.056$ pu · rad

Estimated deceleration area is smaller than the acceleration area ($A_a > A_d$) and, to prevent system instability, the SPS initiates MFV (Fig. 3). The estimated steady-state stability margin in the post-fault state is about $k_{P\%} = 9.8\%$. To restore the 20% stability margin, the SPS initiates SFV (partial closing the main control valves) to obtain $P_{m\infty} = 0.915$ pu. Simulation results are shown in Fig. 9.

It is worth noting that the waveforms in Fig. 10 are very similar to the waveforms in Fig. 9. It means that a short delay in initiation of MFV resulting from the instability prediction by the proposed method has only slight impact on the dynamic response of the power system.

6.7. Remote faults and normal clearing time

As shown in Fig. 7, for remote faults behind the short zones cleared within normal time $t_c = 80$ ms, the system is stable and the SPS should not initiate MFV.

For example, in the event of a 3-phase fault in line L2 at 30% of the line length from the busbars the following values have been obtained:

$P_m = 1$ pu, $P_c = 0.962$ pu, $\Delta\omega = 1.65$ rad/s

$P_{max} = 1.111$ pu, $A_a = 0.044$ pu · rad, $A_d = 0.067$ pu · rad

The estimated deceleration area is larger than the acceleration area ($A_a < A_d$), and the SPS does not initiate MFV (Fig. 3).

The estimated steady-state stability margin in the post-fault state is about $k_{P\%} = 11.1\%$. In order to restore the 20% stability margin, the SPS initiates SFV to obtain $P_{m\infty} = 0.926$ pu by partial closing of the main control valves.

Similar results have been obtained for many other locations of the remote faults.

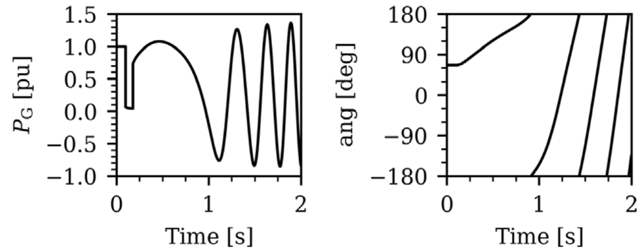

Fig. 11. Waveforms for a 3-phase remote fault in line L2 at a distance of 30% of the line length cleared in delayed time without the use of MFV.

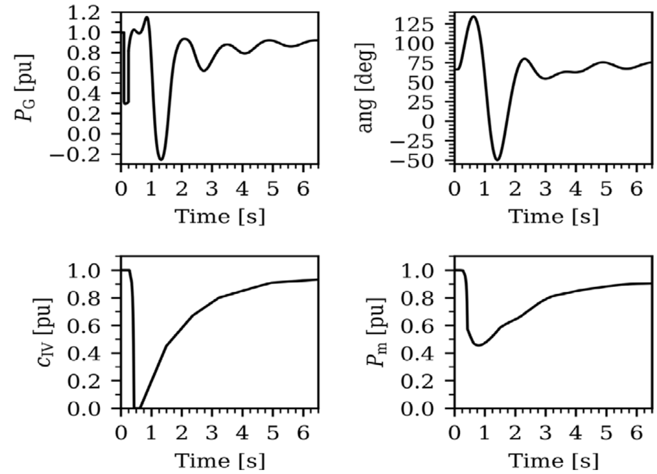

Fig. 12. Waveforms for a 3-phase remote fault in line L2 at a distance of 30% of the line length, cleared in delayed time and MFV initiated by instability prediction without the use of the short-zones option.

6.8. Remote faults and delayed clearing

When a remote fault is cleared with a delayed clearing time (e.g. caused by failure of the main protection), the system may lose transient stability and the SPS should properly predict instability and should initiate MFV. This is illustrated by the example below for a 3-phase fault in line L2 at 30% of the line length from the busbars. The clearing time is assumed to be $t_c = 150\,\text{ms} > t_{CCT}$. In this case, without MFV activation, the generators lose synchronism, which is illustrated in Fig. 11.

In the case considered here, the fault is cleared at $t = 0.1 + t_c = 0.25$ s. For that moment, the following values have been obtained:

$P_m = 1$ pu, $P_c = 0.823$ pu, $\Delta\omega = 3.160$ rad/s

$P_{max} = 1.101$ pu, $A_a = 0.171$ pu · rad, $A_d = 0.058$ pu · rad

Estimated deceleration area is smaller than the acceleration area ($A_a > A_d$) and the SPS initiates MFV.

The waveforms obtained from simulation in the case where MFV is initiated by the SPS are shown in Fig. 12. It is worth noting that the second top of waveform $P(t)$ is larger than the first one due to increased excitation voltage and transient EMF. Shortly after fault clearance, there are deep synchronous swings but, due to fast action of the AVR+PSS, these swings are damped out quite fast.

The estimated steady-state stability margin in the post-fault state is about $k_{P\%} = 10.1\%$. To restore the 20% stability margin, the SPS initiates SFV to obtain $P_{m\infty} = 0.917$ pu by partial closing of the main control valves.

7. Conclusions

This paper addresses the prevention of instabilities in power systems after severe contingencies by fast turbine valving activated by a smart control scheme based on fast real-time instability prediction. The proposed instability prediction method uses local measurements only and is completely different from other methods described in the literature. Our method is based on predicting the magnitude of the power-angle characteristic. Some significant advantages of the proposed method are as follows:

- only local signals measurable in the considered substation are used,
- only simple mathematical operations are required for predicting, which reduces the time needed to generate the signal to initiate the MFV action,
- just after the fault clearance, the method makes it possible to assess the magnitude of the power-angle characteristic in the post-fault state and compute steady-state stability margin,
- when this margin is too small, the SFV action can be initiated as well.

Simulation tests for a large-scale real power system using detailed models of power system elements have confirmed the validity and robustness of the proposed method.

CRediT authorship contribution statement

Sylwester Robak: Conceptualization, Writing – review & editing, Project administration, Funding acquisition. **Jan Machowski:** Methodology, Writing – original draft, Writing – review & editing. **Mateusz Skwarski:** Data curation, Formal analysis, Visualization.

Declaration of competing interest

The authors declare that they have no known competing financial interests or personal relationships that could have appeared to influence the work reported in this paper.

Acknowledgments

This work was supported by the ENERGYTECH-1 project granted by the Warsaw University of Technology through the program Excellence Initiative: Research University (ID-UB).

References

Anon, 2013. PES-TR1 Dynamic Models for Turbine-Governors in Power System Studies. IEEE Power & Energy Society.

Anon, 2016. Ieee std 421.5-2016 (revision of IEEE std 421.5-2005): IEEE recommended practice for excitation system models for power system stability studies.

Cai, Y., Li, W., Zhang, B., Wu, W., Sheng, D., Chen, J., 2017. Reliable Analysis on Fast Valving of Ultra-Supercritical Unit under Transient Fault Conditions, Vol. 2. American Society of Mechanical Engineers, Power Division (Publication) POWER, http://dx.doi.org/10.1115/POWER-ICOPE2017-3230.

CIGRE, 2007. Defense plan against extreme contingencies. CIGRE Technical Brochure No. 316, [Online]. Available: https://e-cigre.org/publication/316-defense-plan--against-extreme-contingencies. (Accessed 09 September 2021).

CIGRE, 2017. Application of phasor measurement units for monitoring power system dynamic performance. CIGRE Technical Brochure No 702.

CIGRE, 2018. A proposed framework for coordinated power system stability control. CIGRE Technical Brochure No 742.

Cong, Y., Regulski, P., Wall, P., Osborne, M., Terzija, V., 2016. On the use of dynamic thermal-line ratings for improving operational tripping schemes. IEEE Trans. Power Deliv. 31 (4), 1891–1900. http://dx.doi.org/10.1109/TPWRD.2015.2502999.

ENTSO-E, 2015. Initial Dynamic Model of Continental Europe, Available: https://docstore.entsoe.eu/publications/system-operations-reports/continental-europe/Initial-Dynamic-Model/Pages/default.aspx.

Karady, G.G., Gu, J., 2002. A hybrid method for generator tripping. IEEE Trans. Power Syst. 17 (4), 1102–1107. http://dx.doi.org/10.1109/TPWRS.2002.805014.

Kobayashi, R., Maekawa, K., Shimomura, K., Sasaki, T., Kowada, Y., Maeda, T., 2011. Development of sequential calculating type autonomous stabilizing controller for maintaining transient stability in case of backup relay operation in load system. IEEE Trans. Power Syst. 26 (3), 1317–1325. http://dx.doi.org/10.1109/TPWRS.2010.2090673.

Kundur, P., 1994. Power System Stability and Control. McGraw-Hill Education Ltd.

Li, X., Ding, L., Zhu, G., Kheshti, M., 2019. Transient instability detection method based on multi-source trajectory information. Int. J. Electr. Power Energy Syst. 113, 897–905. http://dx.doi.org/10.1016/J.IJEPES.2019.06.009.

Lv, J., Pawlak, M., 2019. Additive modeling and prediction of transient stability boundary in large-scale power systems using the Group Lasso algorithm. Int. J. Electr. Power Energy Syst. 113, 963–970. http://dx.doi.org/10.1016/J.IJEPES.2019.05.068.

Machowski, J., Lubosny, Z., Bialek, J., Bumby, J., 2020. Power System Dynamics. Stability and Control, third ed. John Wiley & Sons, New York.

Molina-Cabrera, A., Ríos, M.A., Besanger, Y., Hadjsaid, N., Montoya, O.D., 2021. Latencies in power systems: A database-based time-delay compensation for memory controllers. Electronics (Switzerland) 10 (2), 1–16. http://dx.doi.org/10.3390/electronics10020208.

NERC, 2013. Special protection systems (SPS) and remedial action schemes (RAS), special protection systems (SPS) and remedial action schemes (RAS): Assessment of definition, regional practices, and application of related standards. [Online]. Available: https://www.nerc.com. (Accessed 09 September 2021).

Patel, R., Bhatti, T.S., Kothari, D.P., 2001. Improvement of power system transient stability using fast valving: A review. Electr. Power Compon. Syst. 29 (10), 927–938. http://dx.doi.org/10.1080/15325000152646532.

Pavella, M., Ernst, D., Ruiz-Vega, D., 2000. Transient Stability of Power Systems: A Unified Approach to Assessment and Control. Kluwer Academic.

Pertl, M., Weckesser, T., Rezkalla, M., Marinelli, M., 2017. Transient stability improvement: a review and comparison of conventional and renewable-based techniques for preventive and emergency control. Electr. Eng. 100 (3), 1701–1718, 10.1007/S00202-017-0648-6.

Prioste, F.B., Mendes, P.P.C., Ferreira, C., 2004. Power system transient stability enhancement by fast valving. In: 2004 IEEE/PES Transmission and Distribution Conference and Exposition: Latin America. pp. 639–644. http://dx.doi.org/10.1109/TDC.2004.1432454.

Rebizant, W., Szafran, J., Wiszniewski, A., 2011. Digital Signal Processing in Power System Protection and Control. Springer, ISBN 9780857298027.

Robak, S., Machowski, J., Gryszpanowicz, K., 2018. Automatic alleviation of overloads in transmission network by generation curtailment. IEEE Trans. Power Syst. 33 (4), 4424–4432. http://dx.doi.org/10.1109/TPWRS.2017.2775799.

Robak, S., Machowski, J., Skwarski, M., Januszewski, M., 2020. Improvement of power system transient stability in the event of multi-phase faults and circuit breaker failures. IEEE Trans. Power Syst. 35 (3), 2422–2430. http://dx.doi.org/10.1109/TPWRS.2019.2958110.

Sobbouhi, A.R., Vahedi, A., 2021. Transient stability prediction of power system; a review on methods, classification and considerations. Electr. Power Syst. Res. 190, 106853. http://dx.doi.org/10.1016/J.EPSR.2020.106853.

Wang, H., He, P., 2019. Transient stability assessment and control system for power system. IEEJ Trans. Electr. Electron. Eng. 14 (8), 1189–1196. http://dx.doi.org/10.1002/TEE.22917.

Weber, J., 2015. Description of machine models GENROU, GENSAL, GENTPF and GENTPJ. [Online]. Available: https://www.powerworld.com. (Accessed 09 September 2021).

Wu, X., Xu, A., Zhao, J., Deng, H., Xu, P., 2011. Review on transient stability prediction methods based on real time wide-area phasor measurements. In: DRPT 2011-2011 4th International Conference on Electric Utility Deregulation and Restructuring and Power Technologies. pp. 320–326. http://dx.doi.org/10.1109/DRPT.2011.5993910.

Zhou, Y., Guo, Q., Sun, H., Yu, Z., Wu, J., Hao, L., 2019. A novel data-driven approach for transient stability prediction of power systems considering the operational variability. Int. J. Electr. Power Energy Syst. 107, 379–394. http://dx.doi.org/10.1016/J.IJEPES.2018.11.031.

Zweigle, G.C., Venkatasubramanian, V.M., 2016. Transient instability mitigation for complex contingencies with computationally constrained cost-based control. IEEE Trans. Smart Grid 7 (4), 1961–1969. http://dx.doi.org/10.1109/TSG.2016.2536061.